Supplementary Information for

Photoinduced phase nucleation driven by multiscale charge transfer and symmetry change dynamics

Marius Hervé[1,2]*, Gaël Privault[1,2], Serhane Zerdane[3], Shintaro Akagi[4], Leland B. Gee[5], Ryan D. Ribson[5], Matthieu Chollet[5], Shin-ichi Ohkoshi[2,6], Hiroko Tokoro[2,4], Marco Cammarata[7]*, Eric Collet[1,2,8]*

[1]Univ Rennes, CNRS, IPR (Institut de Physique de Rennes) – UMR 6251; 35000 Rennes, France.

[2]CNRS, Univ Rennes, DYNACOM (Dynamical Control of Materials Laboratory) – IRL 2015, The University of Tokyo; Tokyo 113-0033, Japan.

[3]Paul Scherrer Institute; Villigen, Switzerland.

[4]Department of Materials Science, Faculty of Pure and Applied Sciences, University of Tsukuba; Tsukuba, Ibaraki 305-8577, Japan.

[5]Linac Coherent Light Source, SLAC National Accelerator Laboratory; Menlo Park, CA, USA.

[6]Department of Chemistry, School of Science, The University of Tokyo; Bunkyo-ku, Tokyo 113-0033, Japan

[7]ESRF – The European Synchrotron; 38043 Grenoble Cedex 9, France

[8]Institut Universitaire de France (IUF) ; 75231 Paris, France.

* Email: marius.herve@univ-rennes.fr, marco.cammarata@esrf.fr, eric.collet@univ-rennes.fr.

Supplementary References

1 Yokoyama, T., Tokoro, H., Ohkoshi, S., Hashimoto, K., Okamoto, K. & Ohta, T. Photoinduced phase transition of $RbMnFe(CN)_6$ studied by x-ray-absorption fine structure spectroscopy. *Physical Review B* **66**, doi:10.1103/PhysRevB.66.184111 (2002).

2 Osawa, H., Iwazumi, T., Tokoro, H., Ohkoshi, S., Hashimoto, K., Shoji, H., Hirai, E., Nakamura, T., Nanao, S. & Isozumi, Y. Thermal phase transition of $RbMnFe(CN)_6$ observed by X-ray emission and absorption spectroscopy. *Solid State Communications* **125**, 237-241, doi:https://doi.org/10.1016/S0038-1098(02)00805-0 (2003).

3 Coelho, A. TOPAS and TOPAS-Academic: an optimization program integrating computer algebra and crystallographic objects written in C++. *Journal of Applied Crystallography* **51**, 210-218, doi:doi:10.1107/S1600576718000183 (2018).

4 Hervé, M., Privault, G., Trzop, E., Akagi, S., Watier, Y., Zerdane, S., Chaban, I., Torres Ramírez, R. G., Mariette, C., Volte, A., Cammarata, M., Levantino, M., Tokoro, H., Ohkoshi, S. & Collet, E. Ultrafast and persistent photoinduced phase transition at room temperature monitored by streaming powder diffraction. *Nature Communications* **15**, 267, doi:10.1038/s41467-023-44440-3 (2024).

5 Hervé, M., Akagi, S., Guérin, L., Gee, L. B., Ribson, R. D., Chollet, M., Cammarata, M., Nagashima, S., Ohkoshi, S.-i., Tokoro, H. & Collet, E. Strain-affected ferroelastic domain walls in RbMnFe charge-transfer materials undergoing collective Jahn–Teller distortion. *Rsc Adv* **14**, 35081-35089, doi:10.1039/D4RA06397J (2024).

6 Daniels, J. E., Jones, J. L. & Finlayson, T. R. Characterization of domain structures from diffraction profiles in tetragonal ferroelastic ceramics. *Journal of Physics D: Applied Physics* **39**, 5294, doi:10.1088/0022-3727/39/24/029 (2006).

7 Williamson, G. K. & Hall, W. H. X-ray line broadening from filed aluminium and wolfram. *Acta Metallurgica* **1**, 22-31, doi:https://doi.org/10.1016/0001-6160(53)90006-6 (1953).

8 Scardi, P., Leoni, M. & Delhez, R. Line broadening analysis using integral breadth methods: a critical review. *Journal of Applied Crystallography* **37**, 381-390, doi:10.1107/s0021889804004583 (2004).

9 Felts, A. C., Andrus, M. J., Knowles, E. S., Quintero, P. A., Ahir, A. R., Risset, O. N., Li, C. H., Maurin, I., Halder, G. J., Abboud, K. A., Meisel, M. W. & Talham, D. R. Evidence for Interface-Induced Strain and Its Influence on Photomagnetism in Prussian Blue Analogue Core–Shell Heterostructures, $Rb_aCo_b[Fe(CN)_6]_c\cdot mH_2O@K_jNi_k[Cr(CN)_6]_l\cdot nH_2O$. *The Journal of Physical Chemistry C* **120**, 5420-5429, doi:10.1021/acs.jpcc.5b10761 (2016).

10 Cain, J. M., He, W., Maurin, I., Meisel, M. W. & Talham, D. R. Stimulus induced strain in spin transition heterostructures. *Journal of Applied Physics* **129**, doi:10.1063/5.0045939 (2021).

Supplementary Note 1. Magnetic characterization of $RbMn_{0.94}Co_{0.06}Fe$

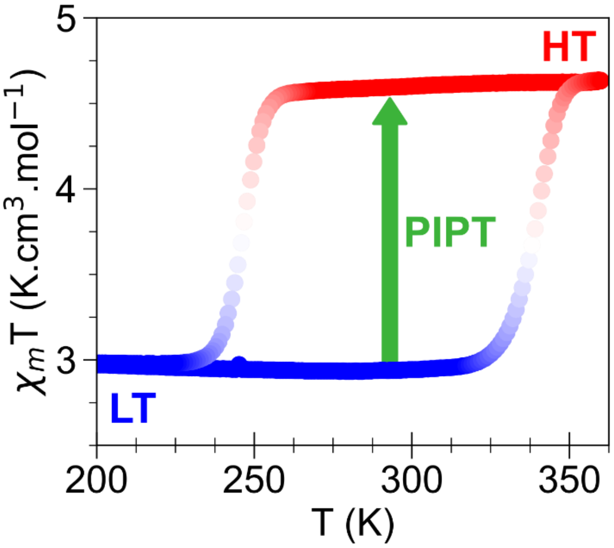

Fig. S1. Bistability regime of $RbMn_{0.94}Co_{0.06}Fe$. $\chi_m T$ vs T plot of the thermal hysteresis in $RbMn_{0.94}Co_{0.06}Fe$.

Supplementary Note 2. Analysis of time-resolved XRD data

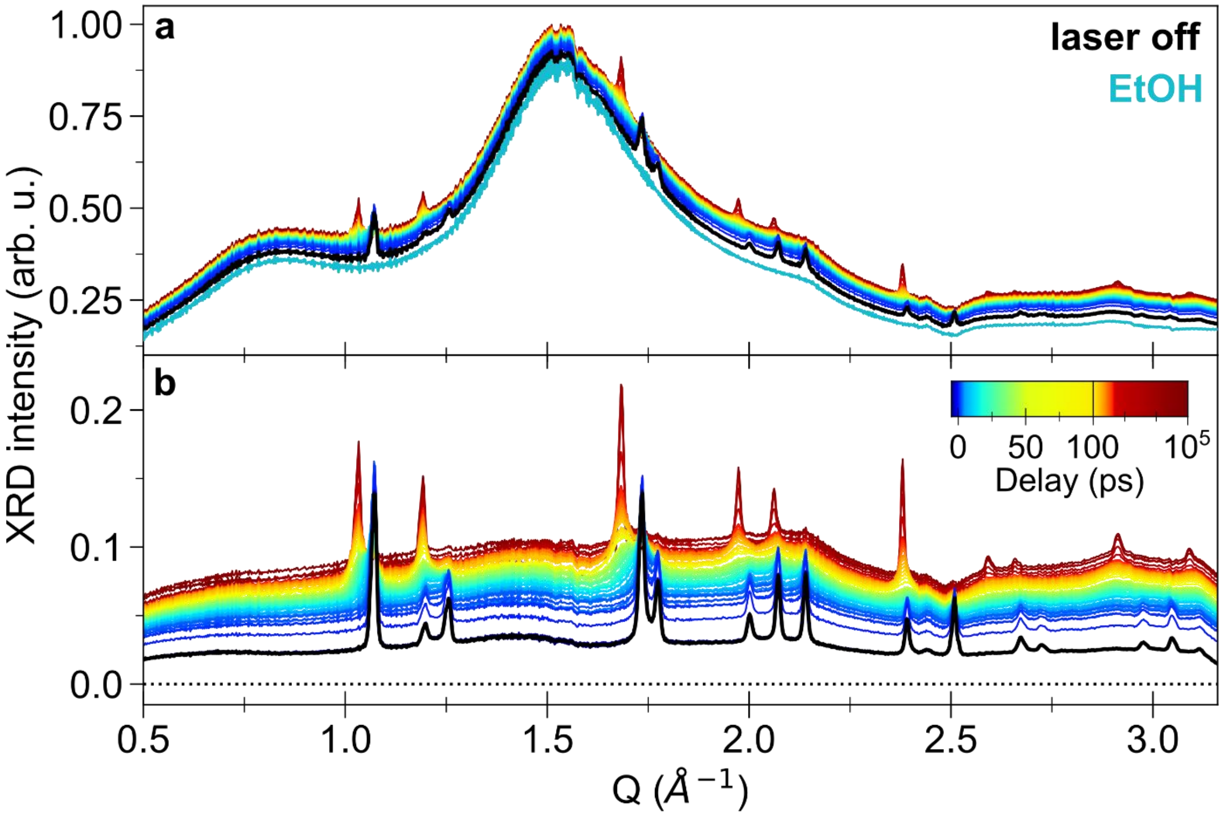

Fig. S2. Solvent subtraction of full XRD patterns. a Full diffraction patterns obtained after azimuthal integration: the XRD pattern of the initial solution is shown in black (without laser irradiation), together with the delay-dependent XRD patterns (see the color bar in panel **b** for the correspondence between delays and colors). The scattering pattern of pure ethanol is also shown (light blue curve), and is subsequently subtracted to all the XRD patterns. **b** Ethanol-subtracted diffraction patterns, without laser irradiation (black curve), and for different delays.

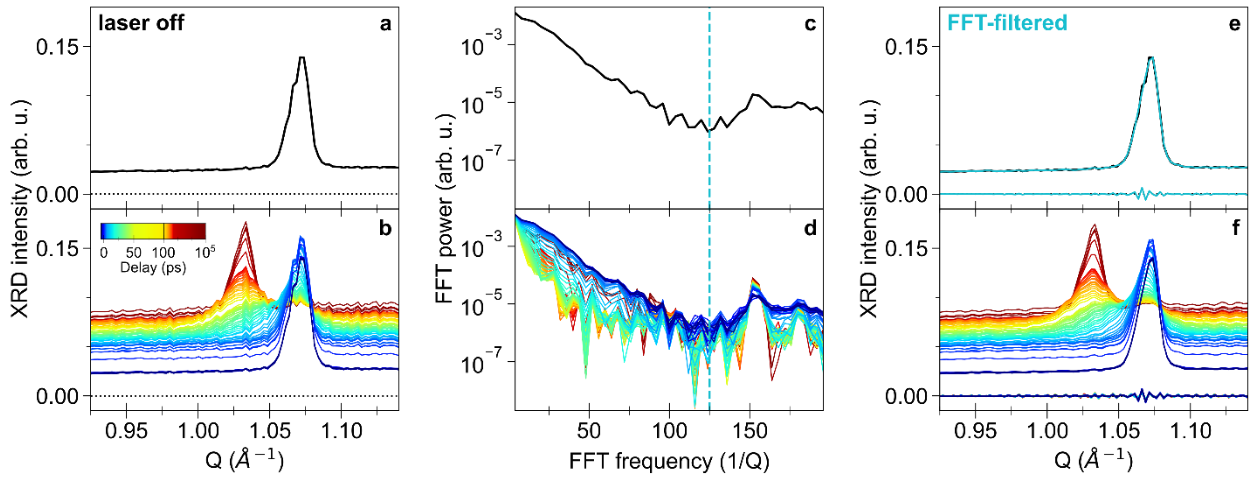

Fig. S3. FFT filter of TR-XRD patterns. Ethanol-subtracted XRD patterns, zoomed around the (111) peak to illustrate the correction applied by the FFT filter, **a** without laser irradiation and **b** for different delays. The FFT of the laser off (**c**) and delay-dependent patterns (**d**) is first calculated, showing a monotonic decrease in amplitude up to high-frequency noise. The FFT amplitude above the defined FFT filter frequency (shown as the light blue dashed curve) is then set to 0 for all the patterns. Inverse FFT is then applied, giving the filtered patterns shown in **e** for laser off (light blue curve) and **f** for the TR-XRD patterns. Panels **e** and **f** also show the filtered intensity, taken as the difference between the FFT-filtered pattern and the corresponding initial one.

Supplementary Note 3. Characterization of RbMn$_{0.94}$Co$_{0.06}$Fe in the streaming powder configuration

To characterize the sample before time-resolved measurements, XRD and XAS measurements were performed for a solution of crystals in the LT and HT phases, separately. The solution with HT crystals was obtained by heating at 350 K a small vial of the initially prepared solution. Figs. 1c and S5a display the XAS spectra of LT and HT crystals, which are characteristic of both phases and of the variation between them, due to the Mn^{3+}-to-Mn^{2+} electronic change[1,2]. Fig. S4 shows the extended XRD patterns of both phases after ethanol subtraction (Fig. S4a) and after background subtraction (Fig. S4b and S4c). To confirm the present experimental scheme, we conducted Pawley refinement of both phases, using the TOPAS-Academic version 6 software[3]. Fig. S4b shows the result for the LT phase (R_{wp} = 9.4 %). The obtained lattice parameters are a_{LT} = 10.0202(7) Å and c_{LT} = 10.5030(9) Å, where the uncertainties correspond to the standard deviation of the associated Pawley fit. For the HT phase (Fig. S4c), the obtained lattice parameter is a_{HT} = 10.5617(3) Å, with R_{wp} = 5.5 %. The present values are very similar to the ones obtained in conventional powder diffraction[4].

As discussed in the Main Text and in[5], ferroelastic domains are observed in the LT crystals, with a size in the 200-600 nm range (average size of 400 nm). A schematic 2D representation of the associated domain structure is also shown in Fig. S4b, that details the one in Fig. 4a. As can be seen, domain walls (DWs) separate domains whose orientation of a_{LT} and c_{LT} differ. In the present cubic-to-tetragonal ferroelastic transformation, it consists of $\{101\}$-type domain walls, oriented here along the diagonal direction. As $a_{LT} \neq c_{LT}$, a gradient of lattice parameters from a_{LT} to c_{LT} is present at the DWs, imposing a strong strain between the domains. This strain is mapped in the XRD pattern by strong peak anisotropies as seen by, e.g., a non-negligible scattering intensity between the (002) and (200) peaks, that are badly accounted for in Pawley refinement (orange arrows in Fig. S4b).

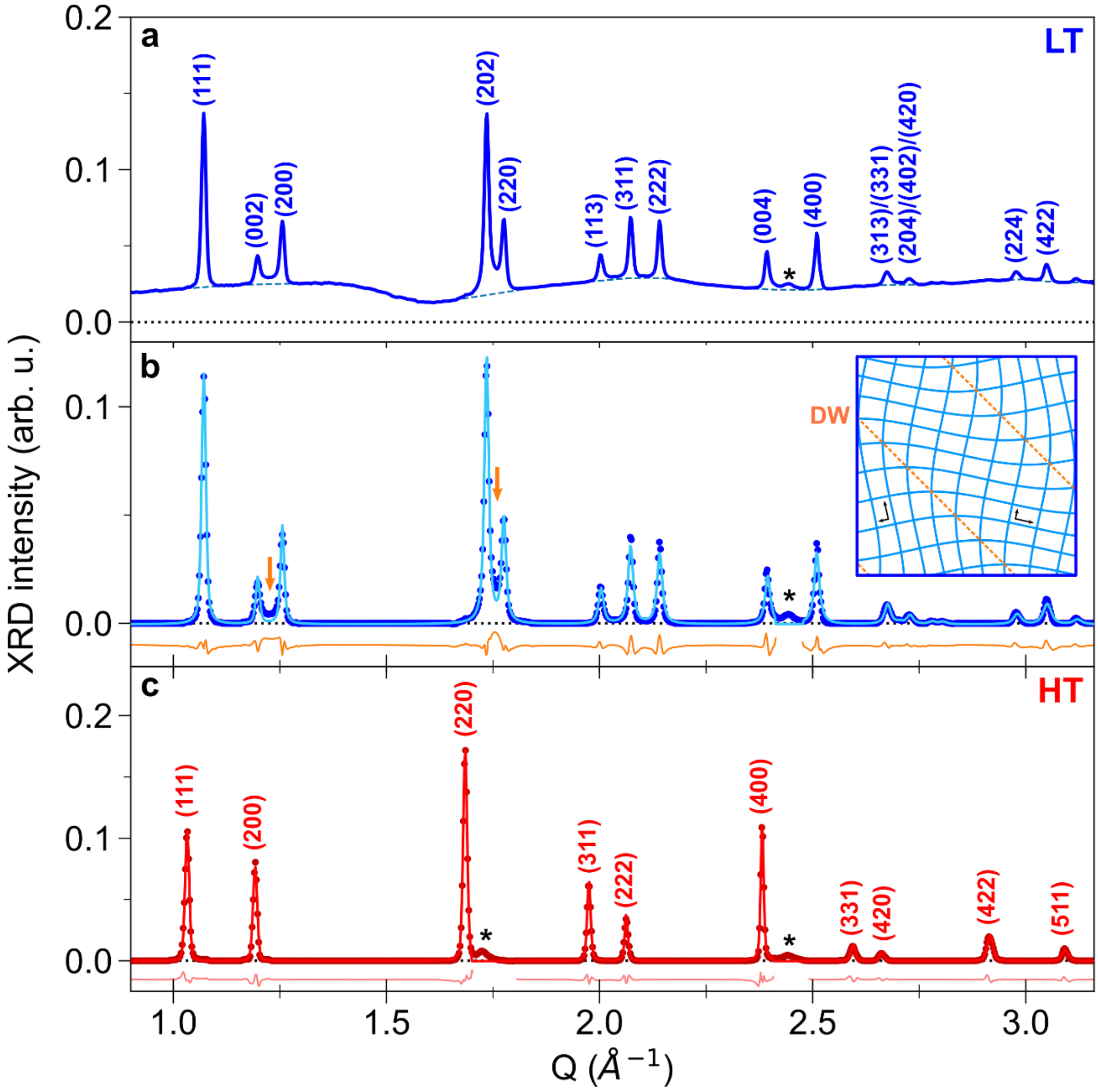

Fig. S4. Pawley refinement of the LT and HT phases in the present experiment. a Full, ethanol-subtracted diffraction pattern of LT crystals, measured in the present experimental configuration. (hkl) Miller indices, indicated in the $F\bar{4}2m$ space group, correspond to the expected Bragg peaks. The asterisk indicates peaks associated to a known, passive impurity in the crystals ($Rb_2Mn^{2+}[Fe^{2+}(CN)_6]\cdot 3.5H_2O$), that forms during the synthesis [4]. The background is then subtracted by fitting a second- or third-order polynomial under each group of peaks (light blue dashed line). **b** Pawley refinement of the LT phase (blue dots), showing the result of the fit (light blue line) and the residuals (orange line, shifted by −0.01). **c** Pawley refinement of the HT phase (red dots), with the result of the fit (red line) and the residuals (light red line, shifted by −0.015). For both phases, the regions corresponding to the impurity are not considered in the refinement. Panel **b** also displays a schematic 2D representation of the domain structure in the initial LT crystals, giving rise to Bragg peak anisotropies that are badly accounted for in Pawley refinement (orange arrows).

Supplementary Note 4. Characterization of the photo-induced state

We also characterized the photo-induced phase of the crystals, reached after photo-excitation of the LT phase. Fig. S5a shows the XAS spectrum measured at a delay of +2 ps, in comparison with the XAS spectra of the LT and HT phases. The corresponding differential signal, taken as the difference between the XAS spectrum at +2 ps and without laser irradiation, is displayed in Fig. S5b. As can be seen, it is very similar to the reference (HT−LT) differential. Therefore, the electronic character reached after 2 ps is already close to the final HT configuration. This confirms that the charge transfer and the associated change from Mn^{3+} to Mn^{2+} occur during this timescale.

To characterize the final phase reached after the dynamics, Fig. S6 shows the XAS spectrum and the full XRD pattern measured at a delay of +100 ns, at high fluences. As can be seen in Fig. S6a, the XAS spectrum is similar to the XAS spectrum of the equilibrium HT phase: the maximum peak corresponds to the Mn^{2+} feature, with a slightly decreased intensity. Fig. S6b shows the Pawley refinement at this delay, in the $F\bar{4}3m$ space group (R_{wp} = 9.5 %). The obtained lattice parameter of the photoinduced cubic phase is a_{PIC} = 10.5681(6) Å, which is very close to the equilibrium HT value (10.5617 Å). A small signature of a remaining tetragonal phase is also observed, due to a residual portion of the sample in the initial LT phase. Overall, these data show that the photo-induced phase corresponds to the HT phase after 100 ns.

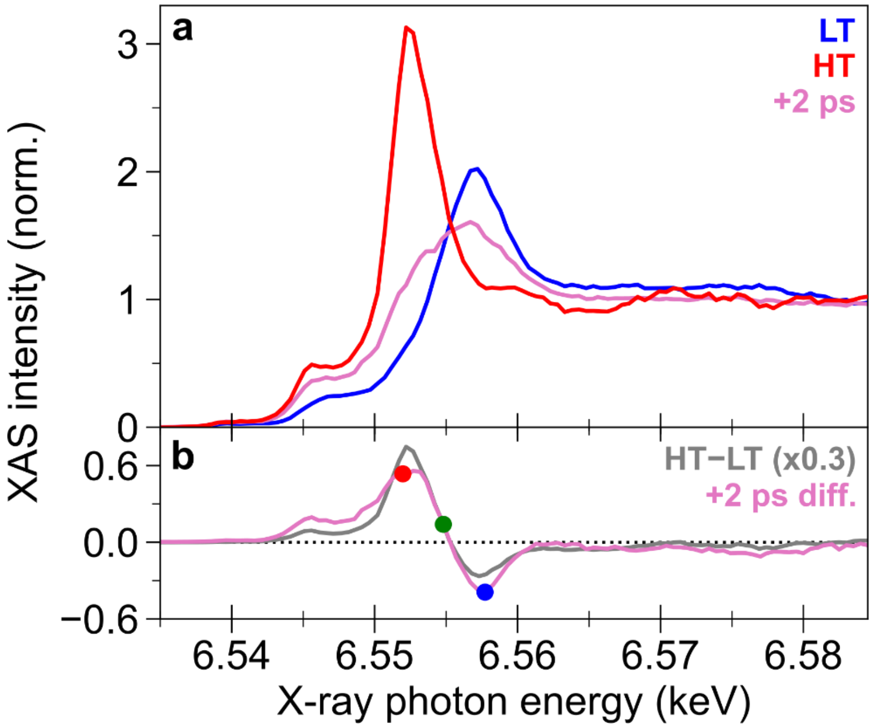

Fig. S5. XAS spectrum at +2 ps. a XAS spectrum at +2 ps, for a laser fluence of 10.0 mJ.cm^{-2} (pink line), compared to the XAS spectrum of the LT and HT phases (blue and red lines, respectively). **b** XAS differential signal at +2 ps (pink line), compared to the (HT−LT) reference differential (grey line, multiplied by 0.3 for the comparison). The red and blue circles indicate the photon energies representative of the Mn^{2+} and Mn^{3+} species respectively, and the green circle is close to the isosbestic point.

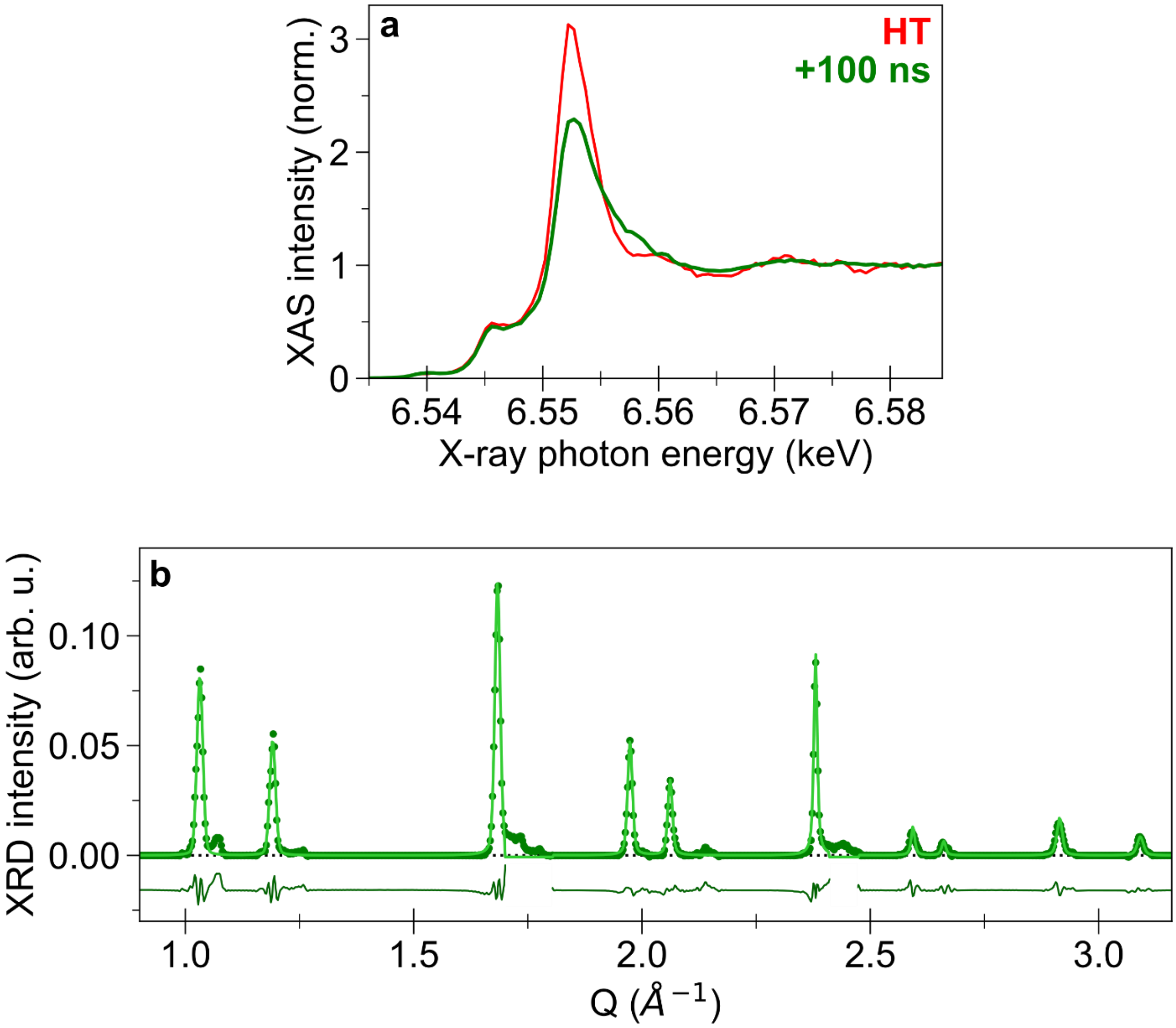

Fig. S6. Characterization of the photo-induced phase at +100 ns. a XAS spectrum at +100 ns, for a laser fluence of 10.0 mJ.cm^{-2} (green line), compared to the XAS spectrum of the HT phase (red line). **b** Pawley refinement of XRD pattern at +100 ns, for a fluence of 16.8 mJ.cm^{-2} (green dots), with the result of the fit (light green line) and the residuals (dark green line, shifted by −0.015). The regions corresponding to the remaining tetragonal phase are not considered in the refinement.

Supplementary Note 5. Time-resolved XRD patterns at different laser fluences

Time-resolved XRD data up to +100 ns were also collected at several laser fluences. Fig. S7 shows the TR-XRD patterns between −5 ps and +100 ns, for 3 different laser fluences. At low fluence (2.2 mJ.cm^{-2}, Fig. S7a), only small changes of the initial LT peaks are observed, including changes in intensity. On the ns timescale, a small peak appears at the equilibrium position of $(111)_{\mathrm{HT}}$ (1.03 Å^{-1}), that is due to the thermal conversion of a fraction of the crystals. At higher fluence, the phase transition dynamics described in this work are observed (Fig. S7b-c). Fig. S7b shows the TR-XRD patterns at a fluence of 10.9 mJ.cm^{-2}, similar to the measurements of the XAS spectra shown in Fig. 1e of the Main Text (10.0 mJ.cm^{-2}). At this fluence, the phase transition occurs on ultrafast timescale, and yields to a phase mixture between a photo-induced HT phase and a remaining LT phase. When increasing the fluence, the photo-induced HT phase becomes dominant, and only a small, residual, fraction of the crystals remains in a tetragonal phase (Fig. S7c and 1f).

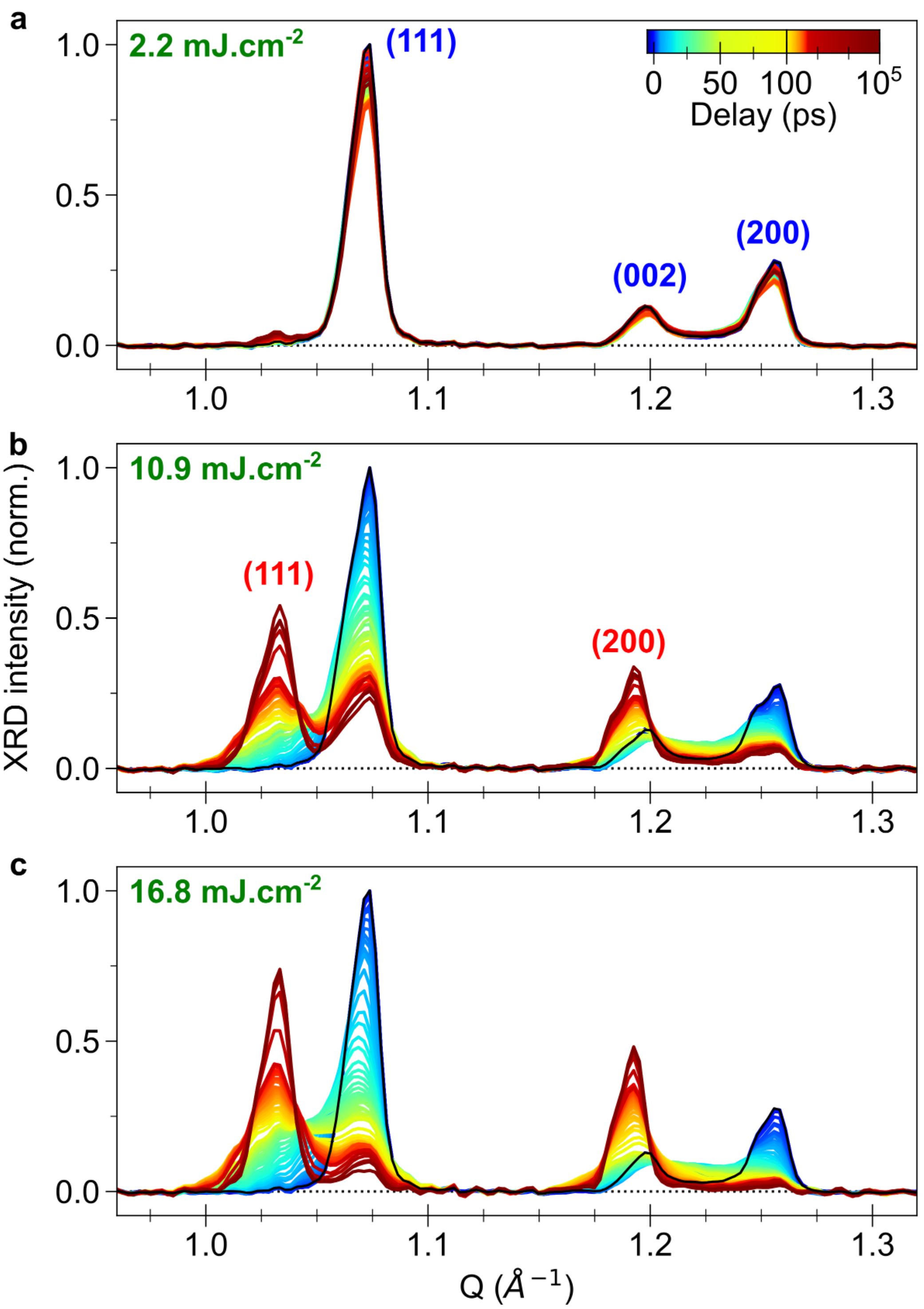

Fig. S7. TR-XRD patterns at different laser fluences. Background-subtracted diffraction patterns between −5 ps and +100 ns, normalized on their maximum, for different laser fluences: **a** 2.2 mJ.cm^{-2}, **b** 10.9 mJ.cm^{-2}, **c** 16.8 mJ.cm^{-2}. The color bar in panel **a** indicates the correspondence between delays and colors, and the diffraction pattern without laser irradiation is also shown (black line).

Supplementary Note 6. Fit of time-resolved XRD for (111) and (002)/(200) peaks

The analysis procedure of TR-XRD patterns was applied separately to the HT and LT (111) peaks (Q-range between 0.9 $Å^{-1}$ and 1.15 $Å^{-1}$) and to the group of HT and LT peaks (002)/(200) (Q-range between 1.11 $Å^{-1}$ and 1.40 $Å^{-1}$). Fig. 1f and Supplementary Videos S1 and S2 show the background-subtracted diffraction patterns, $\left[S(Q,t) - S_{bkg}(Q,t)\right]$, for both groups of peaks. As discussed in the Main Text, the time-resolved evolution of the Bragg peaks contains peak shifts, (asymmetric) broadening and changes in area, that are mapped by the fitting procedure.

Fig. S8 shows the fit result for the (111) Bragg peaks, without laser irradiation and at two typical delays (+45 ps and +1 ns). As can be seen in the fit residuals (grey line), the fitting procedure efficiently captures the different features of the peaks. In particular, it shows that both phases coexist even at short delays (Fig. S8B), and the appearing phase is well described by a Gaussian peak shape within the first hundreds of picoseconds. At longer delays, tiny residuals appear around the final position of the HT peak (Fig. S8C), that are due to the Gaussian model chosen to fit the HT Bragg peak. Indeed, because of the onset of long-range order, the peak width is no longer determined by intrinsic crystal properties (coherence length, strain) but by the instrument resolution, which yields SPV profiles as for the initial LT phase. Nonetheless, this does not affect the global discussion, as the Gaussian model is sufficient to map the dynamics.

The full analysis at all the different delays gives the time dependence of the photoinduced LT and HT (111) peak parameters shown in Fig. S9. As can be seen on Fig. S9a, the residuals of the fit display similar features as in Fig. S8, showing the validity of the analysis. Fig. S9b and S9c display the peak parameters for $(111)_{\mathrm{LT}}$ and $(111)_{\mathrm{HT}}$ respectively. In the case of the initial LT peak, the total peak integral intensity is obtained as $(A_L + A_R)$, and its full width as $(\sigma_L + \sigma_R)$. The mixing fractions $\alpha_{L,R}$ were fixed to the laser off values (Fig. S8a), taken as references. The integral intensity of both peaks was also normalized on the laser off area of the initial LT peak.

The same analysis was also performed for the peaks (002)/(200), where it included two SPV profiles (initial phase) and one Gaussian contribution (appearing HT phase). The result for selected delays is shown in Fig. S10, and the full time-resolved evolution is displayed in Fig. S11. In this case, the appearing contribution evolves from a broad distribution in between the two initial peaks to the final HT peak position (Fig. S11d). As it crosses the initial peak $(002)_{\mathrm{LT}}$, only the area of this peak was set free in the fit (Fig. S11b). For the peak $(200)_{\mathrm{LT}}$ (Fig. S11c), the mixing fractions and $\sigma_R^{(200)}$ were fixed to the laser off values, while the time evolution of $\sigma_L^{(200)}(t)$ maps a residual contribution of the tetragonal phase. The total area of both peaks was also normalized on the total laser off area of both initial LT peaks, namely $\left(A^{(002)_{off}} + A^{(200)_{off}}\right)$.

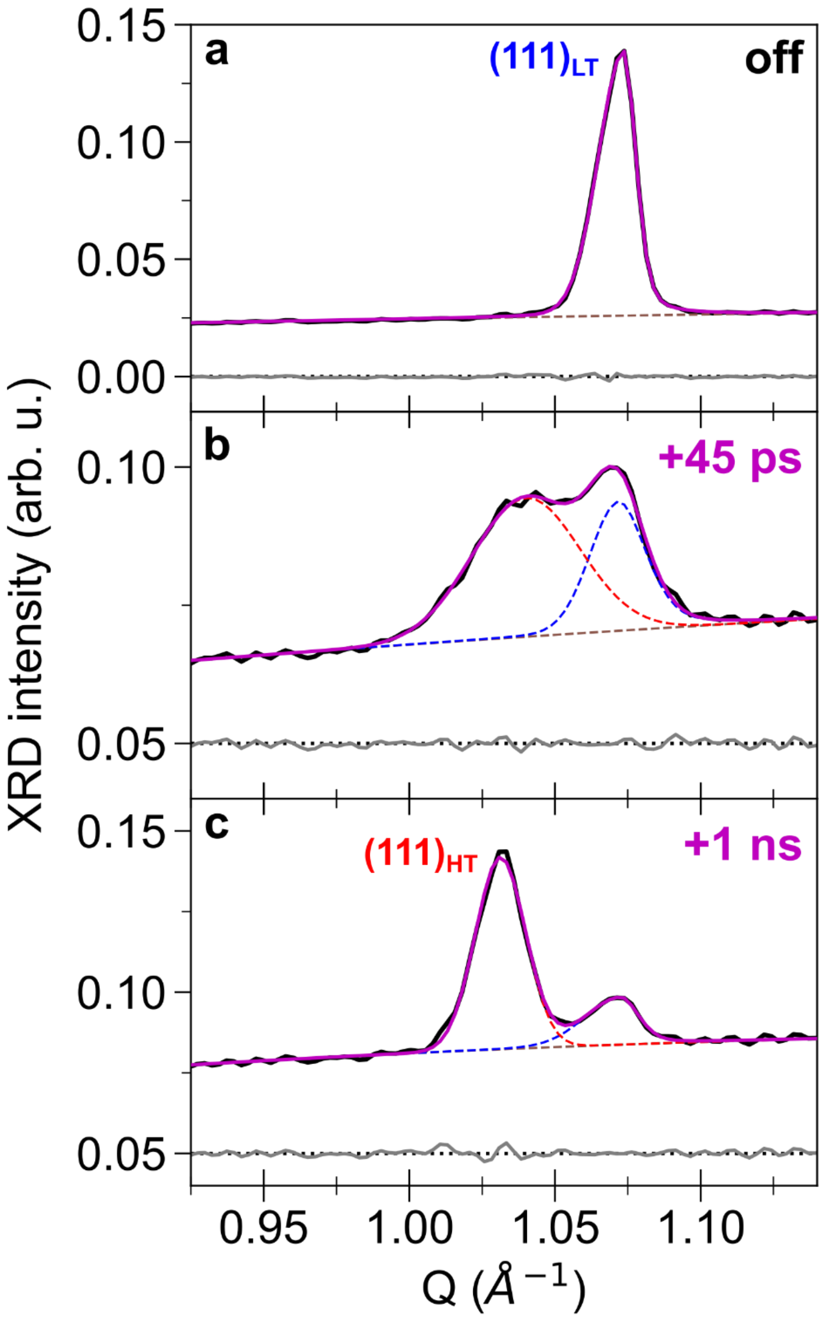

Fig. S8. Individual fits of the peak (111). a Fit of the peak (111) in the initial LT phase (without laser irradiation), with a single SPV profile: the initial pattern (black line) is shown together with the result of the fit ($S_{fit}(Q)$, magenta line), the fitted background ($S_{bkg}(Q)$, brown dashed line) and the residuals of the fit (grey line). **b** and **c** Fit of the same pattern at positive delays (+45 ps and +1 ns, for a fluence of 16.8 mJ.cm^{-2}), where the fit function includes one SPV profile describing the time-evolution of the initial peak (blue dashed line), and one Gaussian profile describing the time-evolution of the appearing phase ($S_{HT}(Q,t)$, red dashed line). In **b** and **c**, the residuals are shifted by +0.05 for clarity.

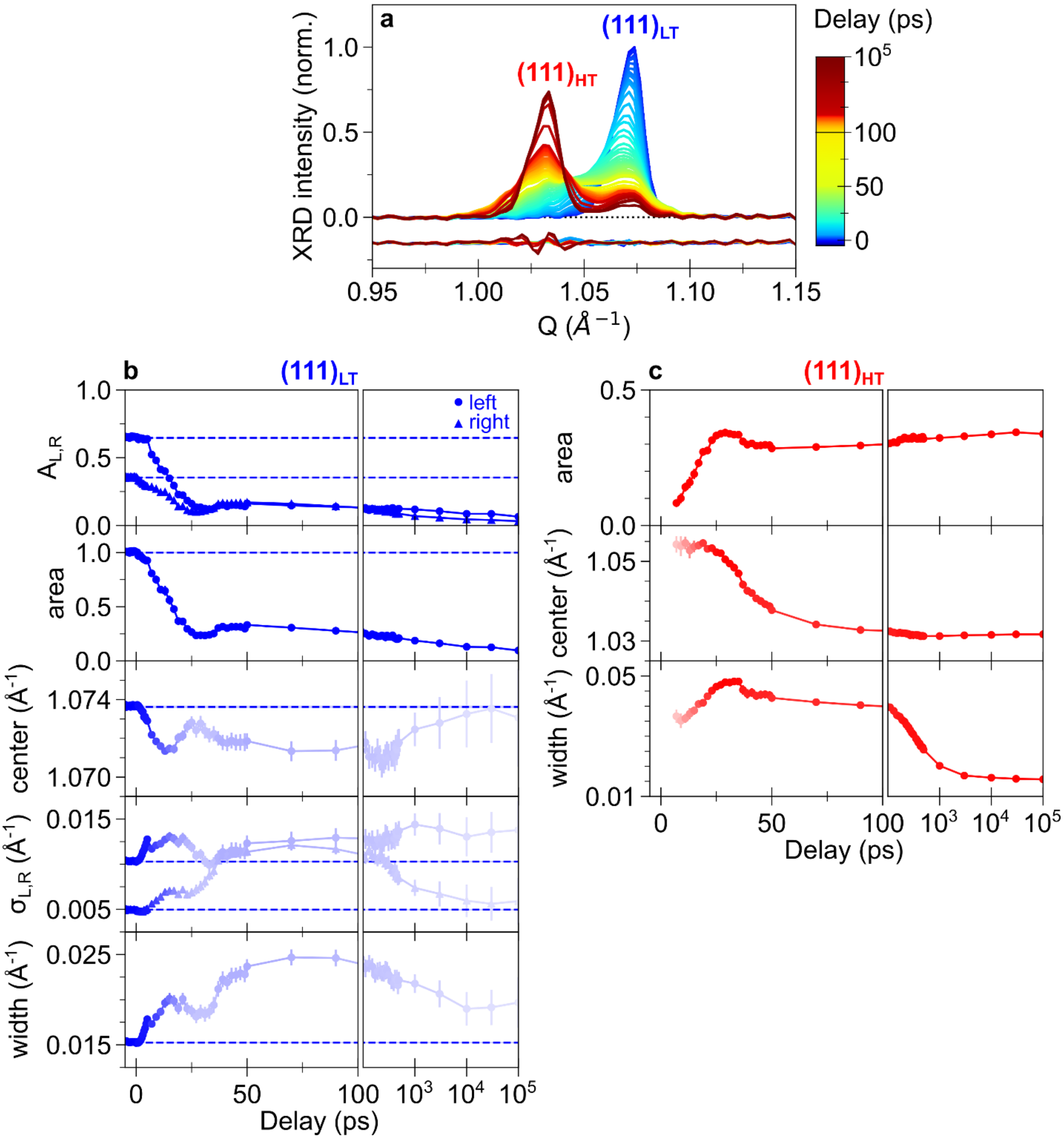

Fig. S9. Time dependence of the fit of (111). a Background-subtracted TR-XRD pattern of (111), normalized on its maximum, for a fluence of 16.8 mJ.cm^{-2}. The residuals of the fit at each delay are also shown, shifted by −0.15. The color bar indicates the correspondence between delays and colors. **b** and **c** Time evolution of the peak parameters resulting from the fit, for (111)$_{LT}$ and (111)$_{HT}$ respectively. For all the parameters except the areas, the color gradient represents the area of the corresponding peak, from white to blue for (111)$_{LT}$, or from white to red for (111)$_{HT}$. For (111)$_{LT}$, the laser off value of each parameter is also shown (blue dashed line), together with its uncertainty (light blue area).

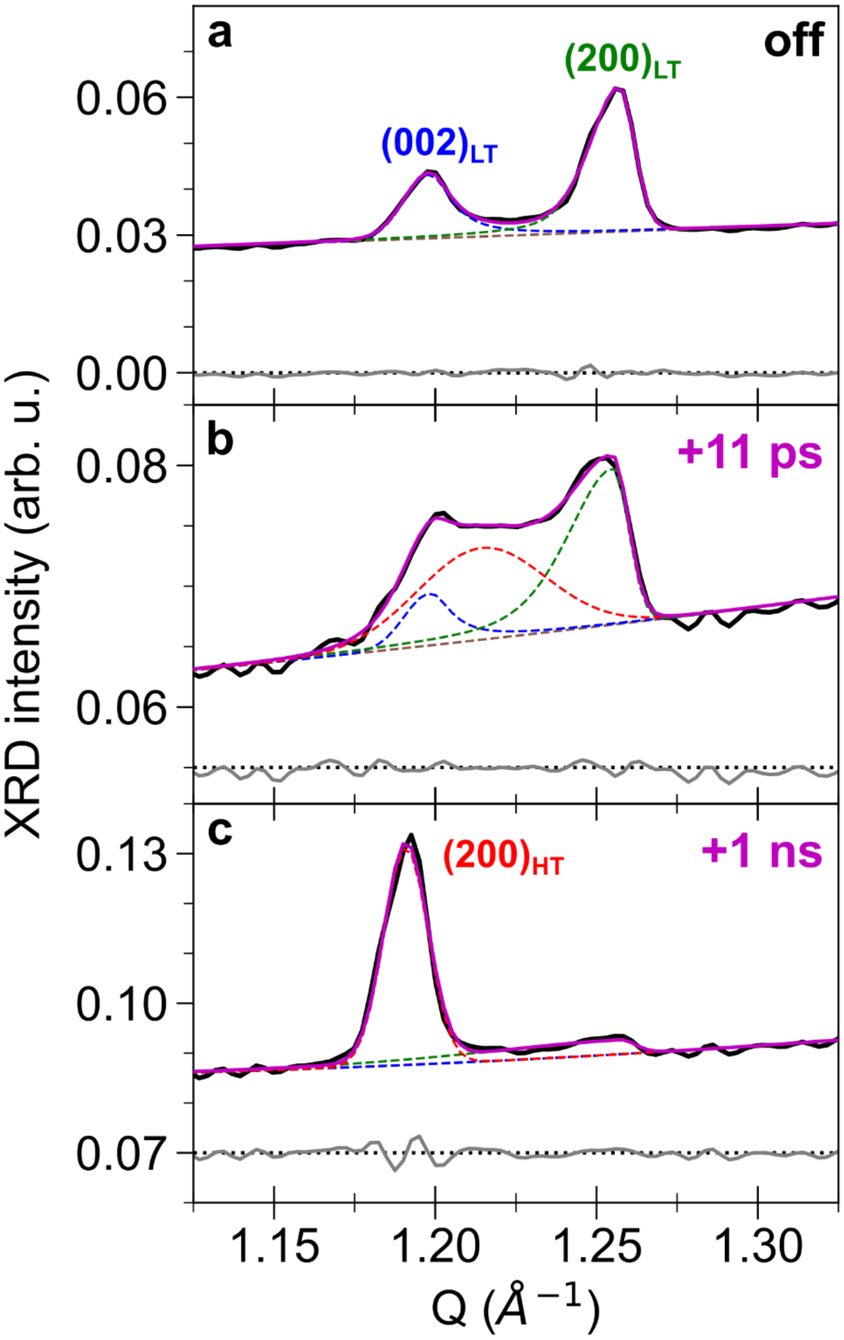

Fig. S10. Individual fits of the group of peaks (002)/(200). a Fit of the two peaks (002) and (200) in the initial LT phase (without laser irradiation), with two SPV profiles: the initial pattern (black line) is shown together with the result of the fit (magenta line), the fitted background (brown dashed line), the two SPV peak profiles (blue and green dashed lines) and the residuals of the fit (grey line). **b** and **c** Fit of the same pattern at positive delays (+11 ps and +1 ns, for a fluence of 16.8 mJ.cm^{-2}), where the Gaussian profile describing the time-evolution of the appearing phase is also shown (red dashed line). In **b** and **c**, the residuals are shifted by +0.055 and +0.07, respectively.

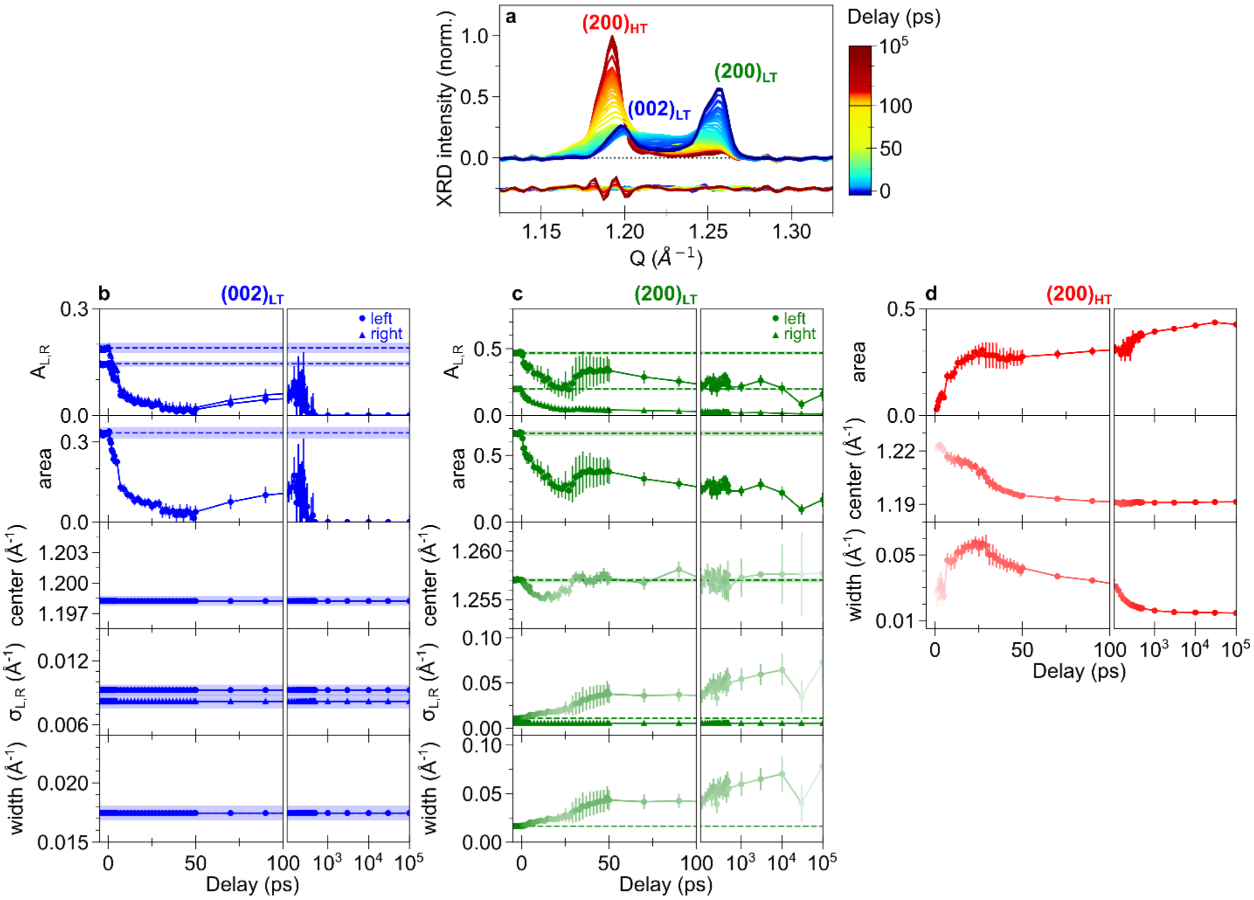

Fig. S11. Time dependence of the fit of (002)/(200). a Background-subtracted TR-XRD pattern of (002)/(200), normalized on its maximum, for a fluence of 16.8 mJ.cm^{-2}. The residuals of the fit at each delay are also shown, shifted by −0.25. The color bar indicates the correspondence between delays and colors. **b**, **c** and **d** Time evolution of the peak parameters resulting from the fit, for the disappearing (002)$_{LT}$ and (200)$_{LT}$ peaks, and the appearing (200)$_{HT}$ peak, respectively. For all the parameters of (200)$_{LT}$ and (200)$_{HT}$ except the areas, the color gradient represents the area of the corresponding peak, from white to green or red. For the LT peaks, the laser off value of each parameter is also shown (dashed line), together with its uncertainty (colored area).

Supplementary Note 7. Strain analysis in time-resolved XRD patterns

As previously discussed, the strain imposed by the domain walls is mapped in the XRD patterns by strong Bragg peak anisotropies. In particular, non-negligible scattering intensity is observed between the (002) and (200) peaks, as a consequence of the gradient of lattice parameters from a_{LT} to c_{LT} around the DWs. The intensity between the (002) and (200) peaks can be further used to quantify the extent of strain in the crystals[5,6]. Indeed, in the hypothetical absence of strain gradient, both (002) and (200) peaks would display symmetric profiles. The deviation from symmetric line shapes thus reflects the extent of strain in the crystals. To quantify it, we artificially constructed symmetrized peak profiles for both peaks, $S_{symm}^{(002)}(Q)$ and $S_{symm}^{(200)}(Q)$, by using the fit parameters of the outer part for each peak (Fig. S13a-b):

$$S_{symm}^{(002)}(Q) = A_L^{(002)}.PV_L^{(002)}(Q)$$

$$S_{symm}^{(200)}(Q) = A_R^{(200)}.PV_R^{(200)}(Q)$$

These two symmetrized peak profiles correspond to hypothetical strain-free, independent domains, as the outer part of both peaks is not affected by the strain gradient. By calculating the deviation from these symmetrized peak profiles, we can then get the XRD signal affected by the DW strain:

$$S_{strain}(Q) = S(Q) - S_{bkg}(Q) - \left[S_{symm}^{(002)}(Q) + S_{symm}^{(200)}(Q)\right]$$

The obtained strain-affected pattern, $S_{strain}(Q)$, is shown in orange in Fig. 1d for the initial LT phase, and its extraction is detailed below in Fig. S13a-b. By integrating $S_{strain}(Q)$ and comparing it to the total integrated signal of (002)/(200), an estimate of the volume fraction of the crystals affected by the DW strain, V_{strain}, is obtained. For the initial phase, it represents $\sim$15 % of the total volume.

This approach was extended to time-resolved measurements, in order to map the temporal evolution of the strain in the crystals. To do so, we performed a fit of the TR-XRD signal of (002)/(200), using $S_{fit}(Q,t)$ as described earlier, with an HT Gaussian fixed below t_0, and free above it. The symmetrized peak profiles are then calculated for each delay:

$$S_{symm}^{(002)}(Q,t) = A_L^{(002)}(t).PV_L^{(002)}(Q,t)$$

$$S_{symm}^{(200)}(Q,t) = A_R^{(200)}(t).PV_R^{(200)}(Q,t)$$

And the strain-affected signal is:

$$S_{strain}(Q,t) = S(Q,t) - S_{bkg}(Q,t) - \left[S_{symm}^{(002)}(Q,t) + S_{symm}^{(200)}(Q,t)\right]$$

The time-dependent strain-affected volume of the crystals is then calculated by integration of $S_{strain}(Q,t)$:

$$V_{strain}(t) = \frac{\int_{Q_0^{(002)}(t)}^{Q_0^{(200)}(t)} S_{strain}(Q,t)\, dQ}{\int S(Q,t)\, dQ} \times 100$$

This analysis was conducted for TR-XRD patterns in the [−1 ps; 6 ps] range, which are shown on Fig. S12. In this delay range, an increase of the scattering intensity in between (002) and (200) is observed, thus corresponding to an increase of the strain in the crystals. Fig. S13c-d shows the strain-affected pattern at a specific delay of +3 ps: its total area is increased compared to the initial strain. The full picosecond evolution of the strain-affected pattern and of the resulting $V_{strain}(t)$ is shown in Fig. S14, as well as in Fig. 2d for different laser fluences.

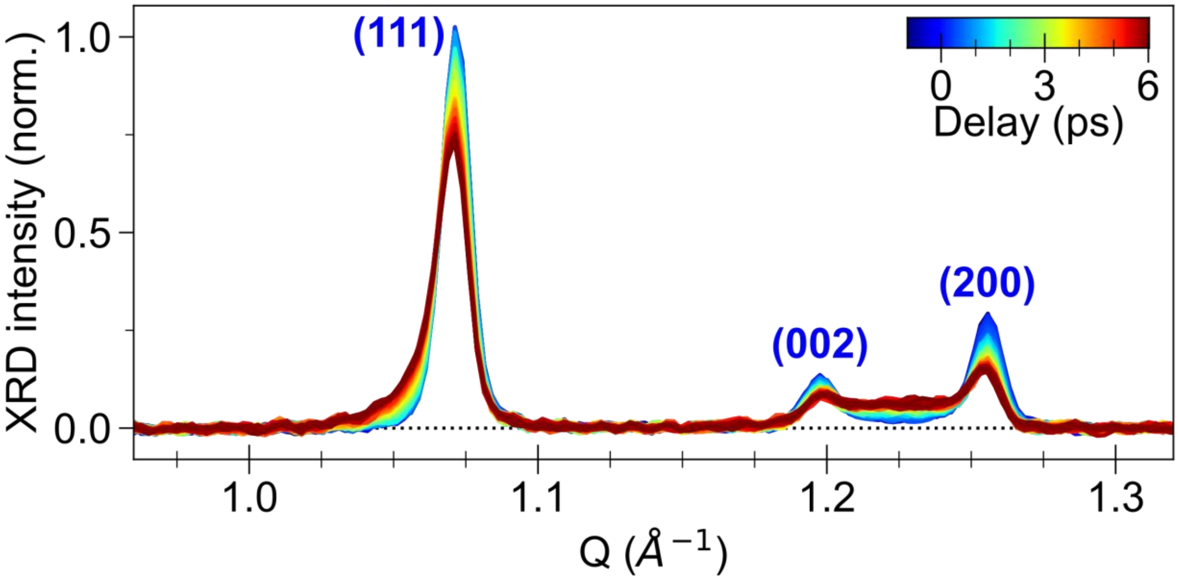

Fig. S12. TR-XRD pattern in the ps range. Background-subtracted TR-XRD pattern between −1 ps and +6 ps, normalized on its maximum, for a fluence of 10.0 mJ.cm^{-2}. The color bar indicates the correspondence between delays and colors.

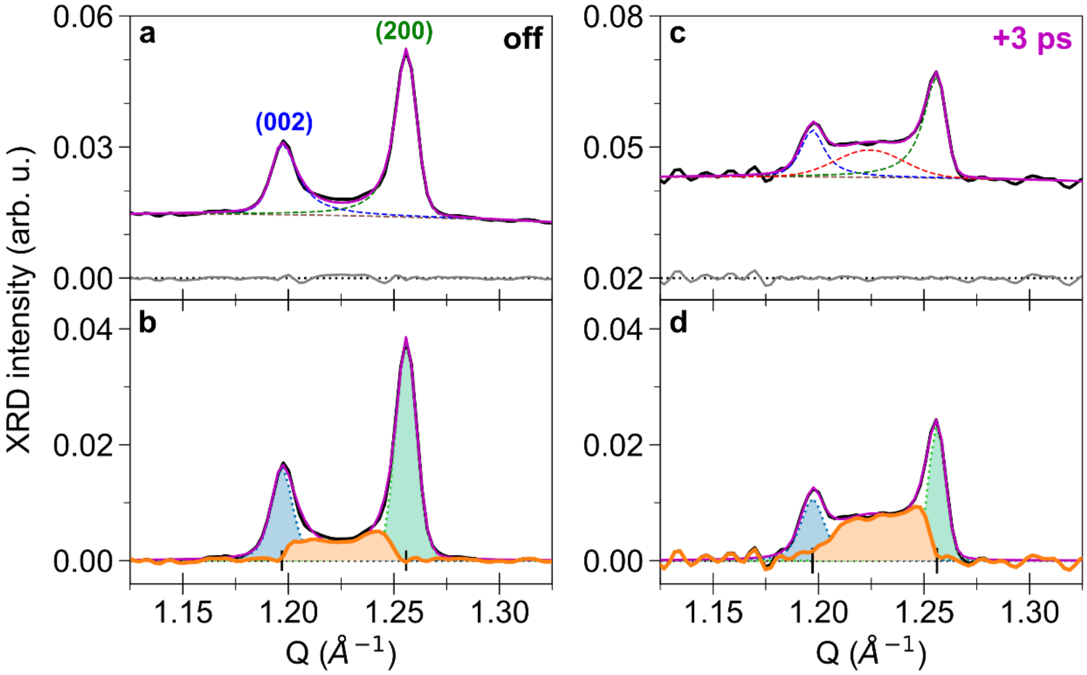

Fig. S13. Strain analysis at specific delays. a Fit of the two peaks (002) and (200) in the initial LT phase (without laser irradiation), as in Fig. S10a: the initial pattern (black line) is shown together with the result of the fit (magenta line), the fitted background (brown dashed line), the two peak profiles (blue and green dashed lines) and the residuals of the fit (grey line). **b** Background-subtracted pattern and its fit, together with the symmetrized peak profiles, $S_{symm}^{(002)}(Q)$ (in light blue) and $S_{symm}^{(200)}(Q)$ (in light green), and the strain-affected pattern (in orange). **c** and **d** Same analysis at a positive delay of +3 ps, for a fluence of 10.0 mJ.cm^{-2}). The Gaussian profile describing the appearing phase is shown as the red dashed line, and the residuals are shifted by +0.02.

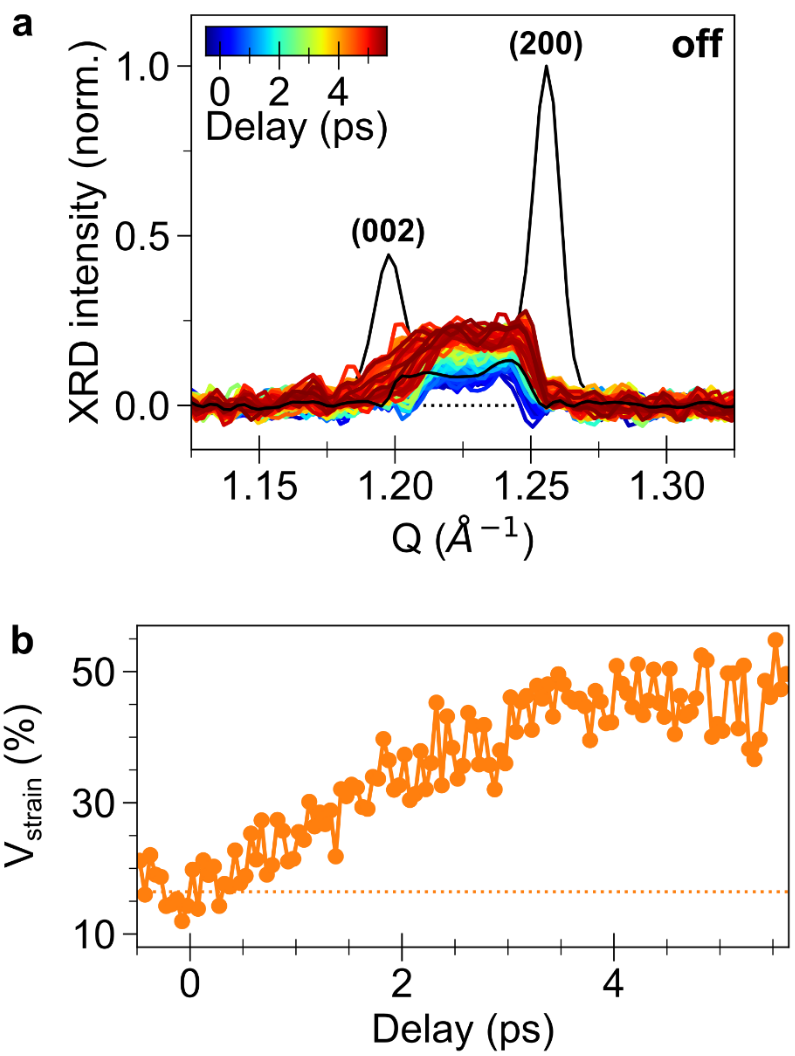

Fig. S14. Strain analysis in the ps range. a Time-dependent strain-affected pattern at a fluence of 10.0 mJ.cm^{-2}, where the delay corresponding to each color is indicated by the color bar. The background-subtracted XRD pattern without laser irradiation, chosen for normalization, is also shown, as well as the associated laser off strain-affected pattern (black lines). **b** Time evolution of $V_{strain}(t)$, extracted from the integration of the patterns in panel **a**. The laser off value of V_{strain} is shown as the orange dotted line.

Supplementary Note 8. Global fit of time-resolved XAS data in the fs-ps range

Fit of the TR-XAS data was first conducted for delay scans in the [−1 ps; 6 ps] range. For this delay range, TR-XAS signal was collected at different X-ray photon energies, and at different laser fluences for the Mn^{2+} photon energy (Fig. 2a-c). Three dominant contributions are observed in the different TR-XAS measurements: an ultrafast evolution in the [0; 200 fs] range, a second contribution up to 500 fs, and a third evolution in the ps range. A global fit with 3 common timescales and a step contribution was thus performed, including all the scans shown in Figs. 2a-c and S15. Given that the sub-200-fs evolution is mostly visible for TR-XAS measurements around the isosbestic energy ($\approx$ 6.555 keV), the first exponential contribution, called thereafter τ_{JT}, was only considered around this photon energy. The two other contributions, τ_{CT} and τ_{pol}, as well as the instantaneous step, were considered for all the scans.

The result of the fit for each TR-XAS measurement is shown in Fig. S15, with the different contributions at play. A very good agreement with the data is observed, confirming that 3 timescales are sufficient to describe the fs-ps dynamics. The obtained timescales are $\tau_{JT} = 47 \pm 16$ fs, $\tau_{CT} = 193 \pm 6$ fs and $\tau_{pol} = 2.1 \pm 0.1$ ps, and the common IRF value is $\sigma_{IRF} = 50 \pm 3$ fs.

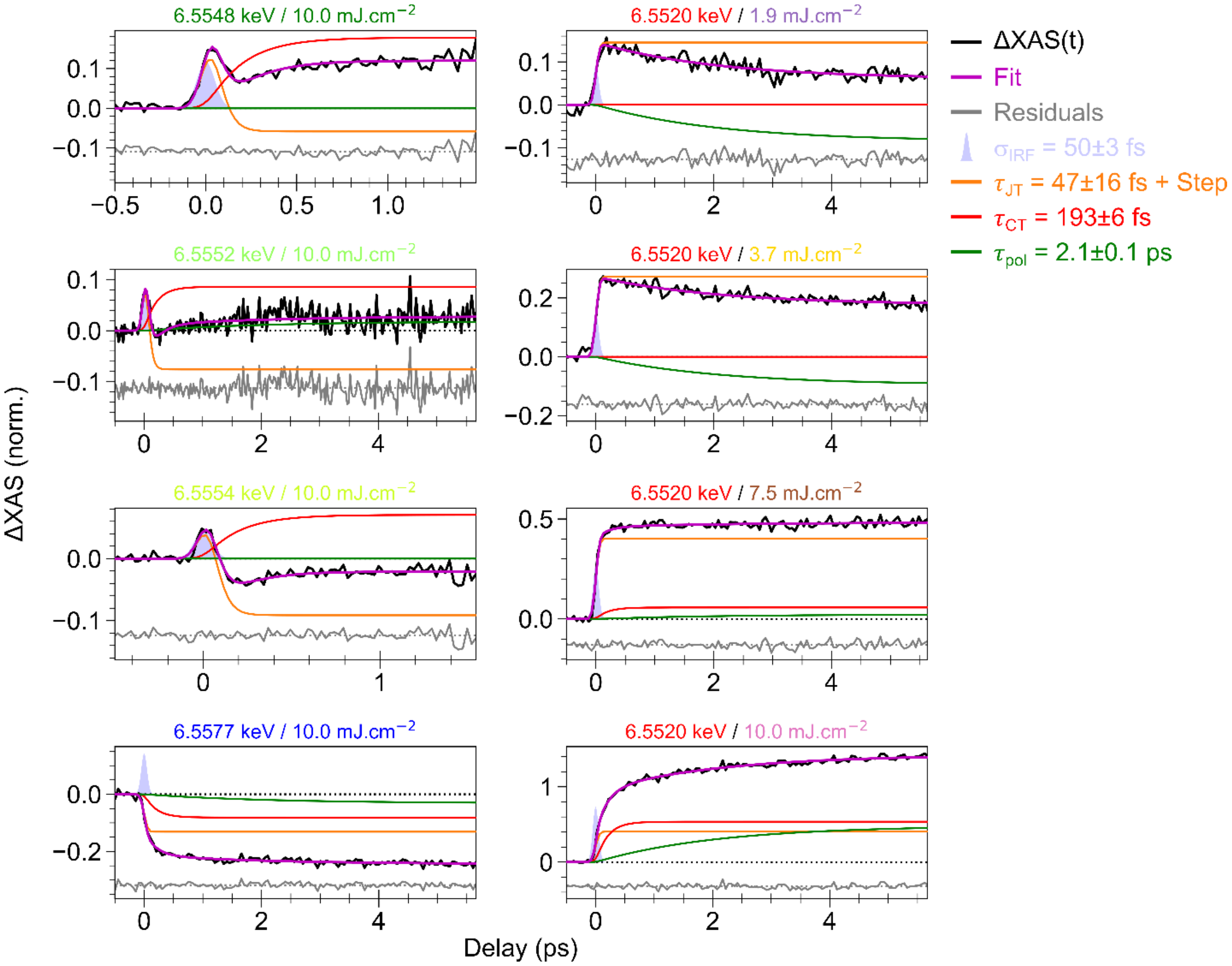

Fig. S15. Fits of TR-XAS in the fs-ps range. Each panel shows the TR-XAS measurement at the photon energy and laser fluence indicated by the label, whose color corresponds to Fig. 2a-c. For each measurement, the XAS signal is shown in black, the associated fit in magenta, and the residuals in grey (shifted for clarity). The three exponential components of the fit are also shown: τ_{JT} contribution, together with the step contribution (orange), τ_{CT} contribution (red), and τ_{pol} contribution (green). The common IRF is shown as the light purple area.

Supplementary Note 9. Global fit of V_{strain} in the ps range

Following the same approach as for the TR-XAS data, a global fit of all the time-resolved evolutions of $V_{strain}(t)$ was also performed. The fit included the time-resolved evolution of V_{strain} for different laser fluences, shown in Fig. 2d. In this global fit, a single exponential timescale was considered (τ_{strain}). The common IRF, as well as t_0 for each scan, were fixed to the values obtained in the global fit of TR-XAS data.

Fig. S16 shows the fit result for the different laser fluences. As can be seen, a single exponential contribution is sufficient to describe the dynamics. The obtained timescale is $\tau_{strain} = 2.04 \pm 0.07$ ps, which is very close from τ_{pol} (2.1 ps) measured in TR-XAS. We thus concluded that the amplification or reduction of Mn^{2+} species on this timescale is concomitant with an increase of strain in the crystals.

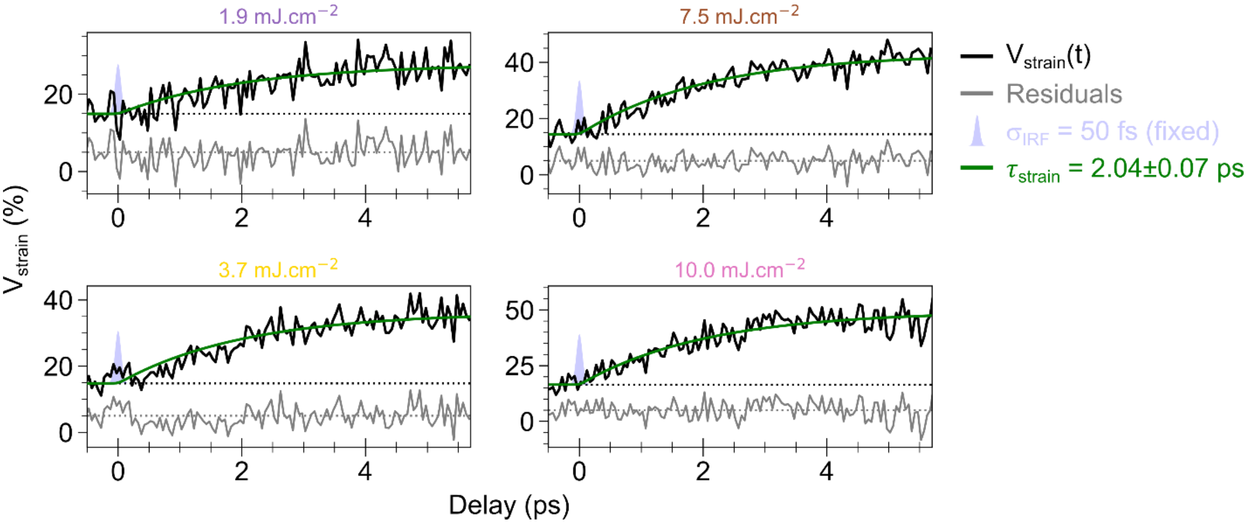

Fig. S16. Global Fit of $V_{strain}(t)$. Fits of $V_{strain}(t)$, measured at the laser fluence indicated by the label, whose color corresponds to Fig. 2d. For each measurement, $V_{strain}(t)$ is shown in black, the associated fit in green, and the residuals in grey (shifted for clarity). The IRF is shown as the light purple area.

Supplementary Note 10. Global fit of time-resolved XAS data in the ps-ns range

In a second step, analysis of TR-XAS data up to +100 ns was conducted. The global fit included TR-XAS measurements at the Mn^{2+} photon energy for different laser fluences, shown in Fig. S17. For all the measurements, 3 contributions are also observed. Within the first ps, an exponential component is measured after an initial increase, similarly to τ_{pol} in the fs-ps measurements. It is followed by a second increase on the [10 ps; 200 ps] range, and further evolution on the ns timescale. We thus performed a global fit of all the measurements with 3 exponential timescales, including τ_{pol} that is fixed to the value obtained in the fs-ps fit (2.1 ps).

Fig. S17 shows the fit result for the different TR-XAS measurements, together with the different contributions at play. As can be seen, a good agreement with exponential functions is also observed on this delay range. The obtained, additional, timescales are $\tau_{exp} = 63 \pm 2$ ps, and $\tau_{eq} = 3.4 \pm 0.3$ ns.

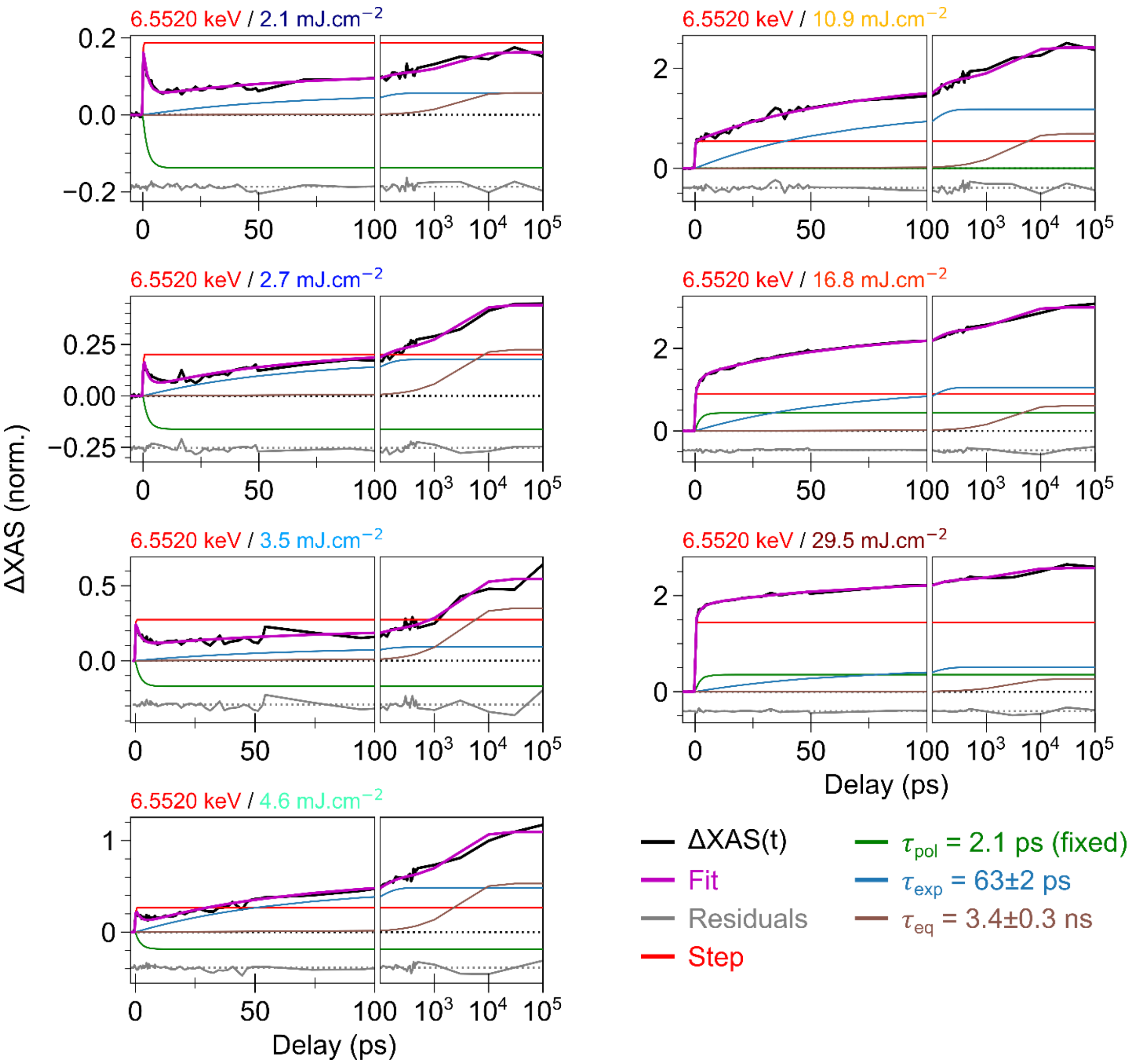

Fig. S17. Fits of TR-XAS in the ps-ns range. Fits of TR-XAS measurements in the ps-ns range, measured at the Mn^{2+} photon energy, for the laser fluence indicated by the label. For each measurement, the XAS signal is shown in black, the associated fit in magenta, and the residuals in grey (shifted for clarity). The three exponential components (τ_{pol} in green, τ_{exp} in blue, τ_{eq} in brown) and the step contribution (in red) are also shown.

Supplementary Note 11. Interpretation of the peak widths in time-resolved XRD

As discussed in the Main Text, broad temporal variations of the peak widths are observed in TR-XRD, spanning multiple timescales (Fig. 3d, S9 and S11). In diffraction measurements, several factors can influence the peak width, including grain size and strain. In the present PIPT mechanism, the strain evolves during the transformation. At the same time, the new phase grows inside the initial LT phase, resulting in variations of the domain size for both phases. Therefore, the time-resolved variations of the strain in the crystals and of the domain size can both impact the peak width as a function of time. To understand this, one can describe the temporal variations of the peak width in a similar way as the Williamson-Hall analysis[7,8], which is commonly used to decouple grain size and strain effects in XRD, including for Prussian Blue Analogues[9,10]. By adapting the Williamson-Hall method to the present case of the appearing HT peaks, well described by a Gaussian profile, the temporal evolution of the peak width can be expressed as:

$$\sigma_{HT}(t)^2 - {\sigma_{instr}}^2 = \left[\frac{2\pi K}{L_C(t)}\right]^2 + [2.\varepsilon(t).Q_{HT}(t)]^2$$

Where σ_{instr} is the instrument resolution function, K is the shape factor of the order of unity, $L_C(t)$ is the diffraction coherence length and $\varepsilon(t)$ the local strain. As such, $L_C(t)$ represents the apparent length of domains along the [hkl] direction of the considered Bragg peak.

This expression is helpful to understand the measured evolution of $\sigma_{(111)}(t)$. As the PIPT progresses, the size of the appearing HT domains keeps increasing. Thus $L_C(t)$ continuously increases with time, and can only be responsible for a decrease of the peak width, from an initially-high value. On the other hand, the strain $\varepsilon(t)$ increases during the 30-ps nucleation, and then decreases with the 60-ps elastic expansion of the crystal. The temporal evolution of $\sigma_{(111)}$ therefore results from the combined effect of $L_C(t)$ and $\varepsilon(t)$. Before 30 ps, the strain increase has more impact on $\sigma_{(111)}$ than the increase of $L_C(t)$, leading to an overall increase of the width. After 30 ps, both $L_C(t)$ and $\varepsilon(t)$ lead to a decrease of $\sigma_{(111)}(t)$, as the strain releases.

Supplementary Videos

Supplementary Video S1. Background-subtracted diffraction pattern of (111) as a function of delay, normalized on its maximum, for a fluence of 16.8 mJ.cm^{-2}.

Supplementary Video S2. Background-subtracted diffraction pattern of (002)/(200) as a function of delay, normalized on its maximum, for a fluence of 16.8 mJ.cm^{-2}.